

HYPERVELOCITY TERMINAL GUIDANCE OF A MULTIPLE KINETIC-ENERGY IMPACTOR VEHICLE (MKIV)

Joshua Lyzhoff* and Bong Wie†

This paper presents the initial preliminary study results of developing a hypervelocity terminal guidance scheme, employing visual and infrared sensors, for a non-nuclear MKIV (Multiple Kinetic-Energy Impactor Vehicle) system that can fragment or pulverize small asteroids (< 150 m) detected with short mission lead times (< 10 years). The proposed MKIV system with its total mass in the range of approximately 5,000 to 15,000 kg is comprised of a carrier vehicle (CV) and a number of attached kinetic-energy impactors (KEIs). Near to a target asteroid, the CV will dispense several KEIs and guide them to hit near-simultaneously different locations widely distributed across the target surface area and to cause shock waves to propagate more effectively through the target body. This paper is focused on developing an image processing algorithm for such coordinated terminal guidance and control of multiple KEIs. GPU-based simulations of a proposed image processing algorithm are conducted to verify the feasibility of impacting a small (< 150 m) asteroid by multiple KEIs. Noiseless as well as noisy visual and IR images are simulated using scaled polyhedron models of 433 Eros and 216 Kleopatra. Preliminary study results indicate that it is technically feasible to impact a small asteroid near-simultaneously at its multiple locations using the proposed MKIV system architecture.

INTRODUCTION

In [1], a Hypervelocity Asteroid Intercept Vehicle (HAIV) system for intercepting an asteroid, at hypervelocity speeds, with a kinetic-energy impactor and delivering a nuclear explosive device (NED) into the created crater, was studied. Further research was conducted on the feasibility of intercepting small (50 - 100 m) asteroids using the HAIV concept with the implementation of a visual or infrared sensor in [2, 3]. General information regarding a kinetic-energy asteroid impact scenario based on energy approximations for dispersing a rubble pile can be found in [4]. Detailed mission feasibility and concept validation simulations were not presented in [4].

A space mission to intercept a comet using a kinetic impactor has been successfully accomplished in the past. NASA's Deep Impact mission used visual cameras and preplanned trajectory maneuvers to intercept Comet 9P/Tempel (Comet Tempel 1). An observer spacecraft performed a flyby of the comet while the impactor spacecraft collided with the comet at 10.2 km/s [5, 6].

On a smaller scale, systems have been designed to intercept ballistic missiles, along with any decoy objects. Missile defense organizations and companies have been developing several innovative

*Ph.D. Graduate Research Assistant, Asteroid Deflection Research Center, Department of Aerospace Engineering, Iowa State University, Ames, IA 50011. Email: jlyzhoff@iastate.edu

†Vance Coffman Endowed Chair Professor, Asteroid Deflection Research Center, Department of Aerospace Engineering, Iowa State University, Ames, IA 50011. Email: bongwie@iastate.edu

solutions to intercepting ballistic missiles in the presence of interceptor decoys [7, 8]. One such example is the Multiple Kill Vehicles (MKVs) designed by Lockheed Martin and Raytheon Company. An MKV system architecture by Lockheed Martin uses a Carrier Vehicle (CV) containing smaller Kill Vehicles (KVs) to intercept ballistic missiles [9, 10]. Several KVs detach from the CV and obtain orientation and position information of themselves as well as the CV. While target acquisition for the KVs is conducted, each KV remains in contact with the CV. Commands calculated by the CV will be distributed to the KVs, which incorporate the decoys or target positions. Each KV has “minimal functionality,” which includes sensors and actuators. A mono-camera system suffers due to the potential of important targets leaving the view of the CV. However, another MKV architecture by Raytheon incorporates a targeting system on each KV, including the CV. All vehicles communicate amongst each other to identify and intercept the ballistic missile, in addition to decoys.

The Multiple Kinetic-Energy Impactor Vehicle (MKIV) concept applied to asteroid disruption is described in [11]. There are two types of the MKIV concept that can be considered: One, where the CV sends guidance commands to the Kinetic-Energy Impactors (KEIs), or two, where each impactor has its own target sensing device and guides itself accordingly. Either concept could be used for a single target or multiple targets. The single target case would have multiple KEIs intercept the single asteroid target. Preliminary MKIV impact simulations using a GPU-accelerated hydrocode are presented in [12].

This paper will focus on an image processing algorithm for such coordinated terminal guidance and control of multiple KEIs. GPU-based simulation results of the proposed image processing algorithm will be discussed to verify the feasibility of impacting a small (< 150 m) asteroid by multiple KEIs. Simulations results using noiseless as well as noisy visual and IR images will be presented for scaled polyhedron models of 433 Eros and 216 Kleopatra. The preliminary results presented in this paper will indicate that it is technically feasible to impact a small asteroid near-simultaneously at its multiple locations using the proposed MKIV system architecture.

NOISELESS IMAGE PROCESSING AND LINE-OF-SIGHT DETERMINATION

The noiseless situation arises in the most ideal image array cases. Consideration of this scenario creates the best case and test bed for calculating line-of-sight (LOS) to the target or targets along with the needed digital image processing. Two cases are considered when impacting an asteroid: single KEI or MKIV with the CV equipped with one asteroid targeting device.

Single Kinetic-Energy Impactor

A single KEI case occurs when only one impactor is sent to intercept and fragment the target. In the noiseless image case, the target may appear as seen in Figure 1. This is a depiction of a scaled 433 Eros, but other scaled models will be used to show the robustness of the multi-impact algorithm. There is no noise associated with the pixels on the image array. Pixel illumination occurs only when signal from the target is present. The center of figure (COF), infrared sensor, or center of bright (COB), visual sensor, may be determined from this image. By using pixel values on the sensor array, the COF and COB are determined as

$$O_{x_{COB}} = \frac{\sum_{i=1}^{y_{pix}} \sum_{j=1}^{x_{pix}} G(i, j) j}{n_{pix}} \quad \text{if } G(i, j) \geq \xi_{COB} \quad (1)$$

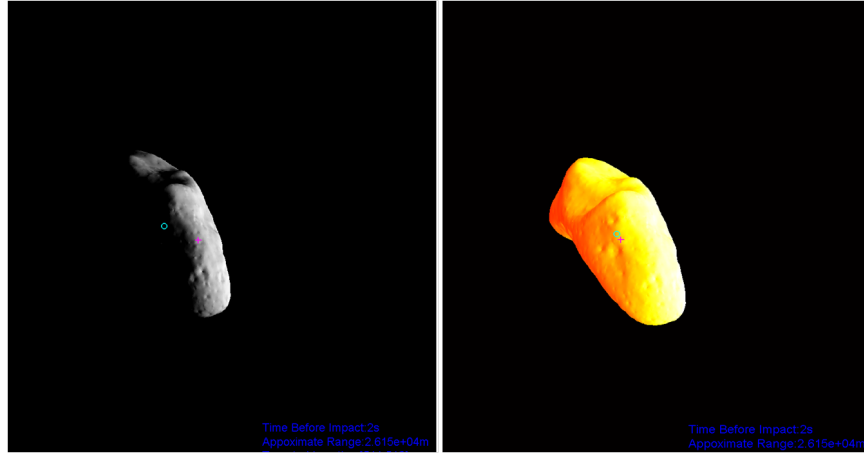


Figure 1: Noiseless visual (left) and IR (right) images of 433 Eros used for terminal guidance simulation.

$$O_{yCOB} = \frac{\sum_{i=1}^{y_{pix}} \sum_{j=1}^{x_{pix}} G(i, j) i}{n_{pix}} \quad \text{if } G(i, j) \geq \xi_{COB} \quad (2)$$

$$O_{xCOF} = \frac{\sum_{i=1}^{y_{pix}} \sum_{j=1}^{x_{pix}} j}{n_{pix}} \quad \text{if } G(i, j) \geq \xi_{COF} \quad (3)$$

$$O_{yCOF} = \frac{\sum_{i=1}^{y_{pix}} \sum_{j=1}^{x_{pix}} i}{n_{pix}} \quad \text{if } G(i, j) \geq \xi_{COF} \quad (4)$$

where O_x and O_y are the IR or visual image's horizontal and vertical centroid pixel location, x_{pix} is the horizontal number of pixels, y_{pix} is the vertical number of pixels, i is horizontal pixel location, j is vertical pixel location, $G(i, j)$ is value of image at horizontal and vertical pixel coordinate, and ξ_{COB} and ξ_{COF} are an image pixel minimum inclusion limit. This limit will be significant when calculating COB and COF for an image with the inclusion of noise. For simplicity, in later sections the subscripts of COB and COF are dropped due to the estimation of multiple impact locations.

Multiple Kinetic-Energy Impactors

The MKIV architecture explores the use of a single spacecraft platform which detaches multiple KEIs. Each KEI communicates with the main spacecraft, called the CV. Due to communication, the CV is the only spacecraft that is required to carry an asteroid targeting sensor device. Doing so will cause multiple KEIs to impact over the asteroid's surface and cause distributed damage. These varying locations of impact are difficult to determine when the shape of the target is not well known. However, these locations can be found by implementing image processing.

KEI Impact-Location Determination

When an image of a target body is obtained, the target-body image has to be split into chunks according to the size of the asteroid, the orientation, and the number of KEIs impacting the target. The COB or COF locations found previously separate the image into either the upper and lower

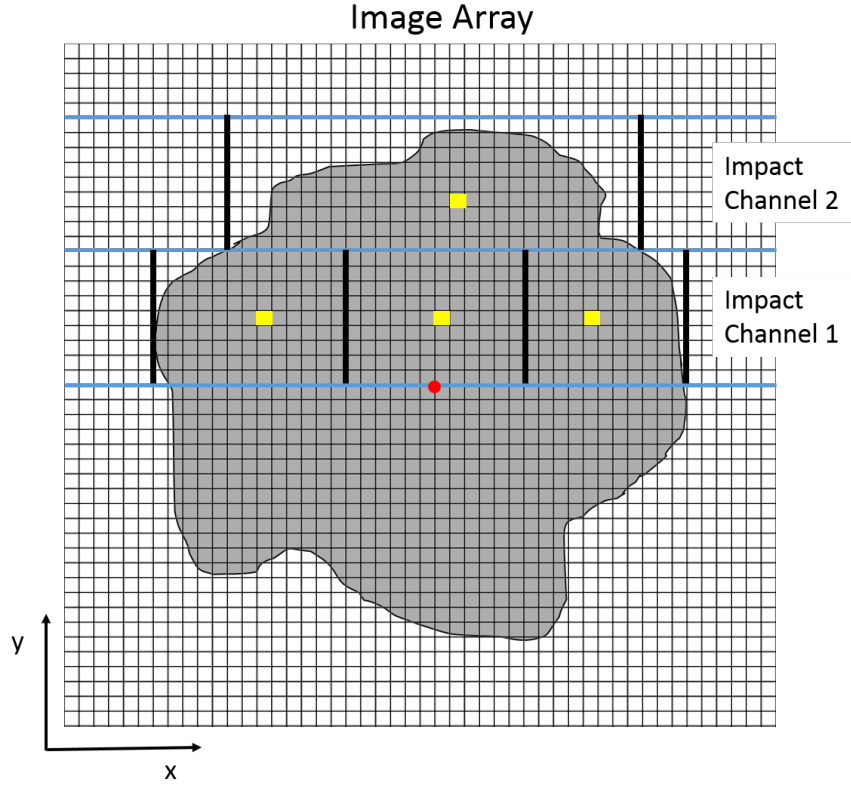


Figure 2: Upper image analysis for a 9-impact situation (1 CV and 8 KEIs). Red square indicates the COF and CV impact location, blue horizontal lines indicate the impact channel boundaries, black vertical lines are the chunk centroiding boundaries, and yellow rectangles are KEI impact locations. Image is not proportionate to actual situation.

image (horizontal split) or the left and right image (vertical split). To determine whether the image is split horizontally or vertically, the following criterion must be met

$$\frac{y_{max} - O_y}{x_{max} - x_{min}} \geq \frac{1}{2} \quad (\text{horizontal split}) \quad (5)$$

where y_{max} is maximum vertical pixel that the asteroid fills in the upper half of the image, and x_{min} and x_{max} are the minimum and maximum horizontal pixels that are filled by the asteroid. If this criterion is not met, the image is split vertically.

Once the image has been split, the number of impact channels can be determined, along with the half-image asteroid pixel fill. Impact channels limit the number of rows on the asteroid's image that the impactors will be allowed to impact in. The maximum number of channels can be calculated as

$$N_{Channel} = \frac{N_{cr} - 1}{2} - \text{FLOOR}\left(\frac{N_{cr} - 1}{4}\right) \quad (6)$$

where $N_{Channel}$ is the number of impact channels and N_{cr} is the number of impactor spacecrafts. This equation only holds when there are an odd number of impactors, which includes the main body impactor impacting at the center of figure of the target. For a general purpose, Equation 6 can

be used for the total number of impact channels. The number of impactors in each channel can be calculated as

$$N_{k_{craft}} = \text{NINT} \left(\frac{A_{k_{Channel}}(N_{cr} - 1)}{2 A_{half}} \right) \quad (7)$$

where $N_{k_{craft}}$ is the number of impactors in the k^{th} channel, $A_{k_{Channel}}$ is the pixel area of the k^{th} channel, and A_{half} is the pixel area of the asteroid on half the image.

Once the number impactors are determined for each channel, the impact location can be calculated. Dividing the k^{th} channel area by the number of k^{th} channel impacting spacecrafts results in an impact area estimation. This area is the criterion for placing an impact location. The algorithm sums the asteroid's image filled pixels in each channel. After the pixel area reaches the divided channel's area, an impact location is placed in the centroid of the channel sector. The centroid estimation for the channel sector and the upper half of the image is then processed as

$$O_x(k, N) = \frac{\sum_{j=x_{sN}}^{x_{eN}} \sum_{i=O_y+(k-1)\frac{y_{max}}{N_{Channel}}}^{O_y+k\frac{y_{max}}{N_{Channel}}} j}{(x_{eN} - x_{sN}) \left(\frac{y_{max}}{N_{Channel}} \right)} \quad \text{if } G(i, j) \geq \xi \quad (8)$$

$$O_y(k, N) = \frac{\sum_{j=x_{sN}}^{x_{eN}} \sum_{i=O_y+(k-1)\frac{y_{max}}{N_{Channel}}}^{O_y+k\frac{y_{max}}{N_{Channel}}} i}{(x_{eN} - x_{sN}) \left(\frac{y_{max}}{N_{Channel}} \right)} \quad \text{if } G(i, j) \geq \xi \quad (9)$$

$$\mathbf{d}_{k,N} = \begin{bmatrix} \frac{2H O_x(k,N)}{x_{pix}} - H \\ \frac{2H O_y(k,N)}{y_{pix}} - H \\ 0 \end{bmatrix} \quad (10)$$

where k is the channel number, N is the KEI number within the channel, x_{sN} is the starting x -value pixel for the N^{th} spacecraft impact location in the k^{th} channel, x_{eN} is the ending x -value pixel for the N^{th} spacecraft impact location in the k^{th} channel, H is half of the view width, in meters, corresponding to range to the target and the field of view of the camera, and $\mathbf{d}_{k,N}$ is the deviation vector for each impactor intercept location in the camera frame. The starting location of the $(N+1)^{\text{th}}$ spacecraft, in general, is the ending x -value for the N^{th} spacecraft. Note, this is the formulation for only the upper half of the image. A similar process can be done for the bottom of the image and when the image is separated into right and left instead of upper and lower halves. A depiction of the impact channels, channel subdivision, and centroiding corresponding to an upper and lower half split can be seen in Figure 2.

Once an impact location is calculated for all impactors, the locations need to be related to the corresponding LOS. This is simply done by taking the coordinates of the centroids and transforming them into the inertial reference frame. The estimated LOS pointing vector for each spacecraft is then

$$\hat{\lambda} = \frac{\mathbf{r}_T - \mathbf{r}_{sc_{k,N}} + C^{I/A} \mathbf{d}_{k,N}}{\|\mathbf{r}_T - \mathbf{r}_{sc_{k,N}} + C^{I/A} \mathbf{d}_{k,N}\|} \quad (11)$$

where \mathbf{r}_T is the target's estimated location in the inertial frame, $\mathbf{r}_{sc_{k,N}}$ is the inertial location of the N^{th} impactor spacecraft in the k^{th} channel, and $C^{I/A}$ is the transformation matrix from the camera frame, A , to the inertial frame, I .

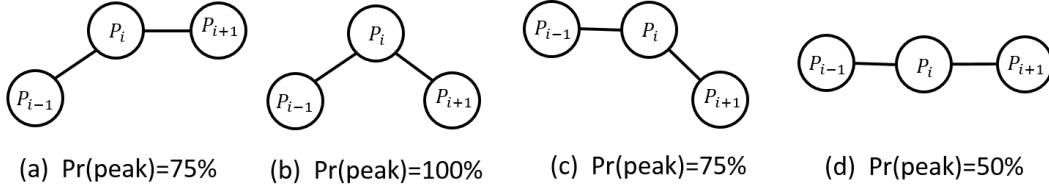


Figure 3: Probabilities of each binned histogram location point, P_i . All other combinations not listed result in a 0% peak probability

IMAGE PROCESSING AND LOS DETERMINATION WITH NOISE

Gaussian random noise, with zero mean, is added to the noiseless image, G , using a conversion of a random uniform distribution to random normal distribution by Box-Muller transform [14]. The standard deviation of the noise is determined from the amount of electrons excited by the target and device parameters. Such parameters and processes can be found in [13]. Once the full image is simulated, the actual object on the image plane must be detected and other image noise eliminated. Once the objects are detected, the targeting of the asteroid is the same as the noiseless system.

Object Detection and Elimination of Noise

The noisy image, W , is first subjected to a median filter, converted into greyscale, and then converted into a binary image. Otsu's method is used to determine an initial thresholding limit, P_o . The values of the greyscale image (GSI) range from 0 to 255, and the values for the normalized greyscale image (NGSI) range from 0 to 1. Otsu's method is described in detail in [15]. However, in most cases, Otsu's method finds a lower thresholding limit than what is desired when trying to eliminate noise. A solution is to use Otsu's method threshold value, which is normalized by 256, to help find a higher threshold. By binning the GSI information into a 32 bin collection, peaks may be found. Figure 3 depicts how to decide if the histogram value is a peak, which is similar to [16], where histogram valleys are found. If the peak falls into the probability being greater or equal to 75 percent, this location within the binned histogram is considered a peak. Once each peak is determined, a value of interest is found as

$$\bar{P}_b = \frac{1}{32n} \sum_{i=1}^n P_b(i) \quad (12)$$

where P_b is the value at which a peak occurs in the binned histogram, n is the number of peaks, and \bar{P}_b is the average of the peak locations. This value ranges from 0 to 1, hence the division by the binned size value. If, however, there are no peaks, \bar{P}_b can be estimated using a variable which will be discussed later.

The overall average of the NGSI is computed as

$$\bar{P} = \frac{1}{x_{pix} y_{pix}} \sum_{j=1}^{x_{pix}} \sum_{i=1}^{y_{pix}} W_n(i, j) \quad (13)$$

where \bar{P} is the average value of the image array, and W_n is the filtered NGSI. By using \bar{P} , an upper threshold estimate can be obtained as

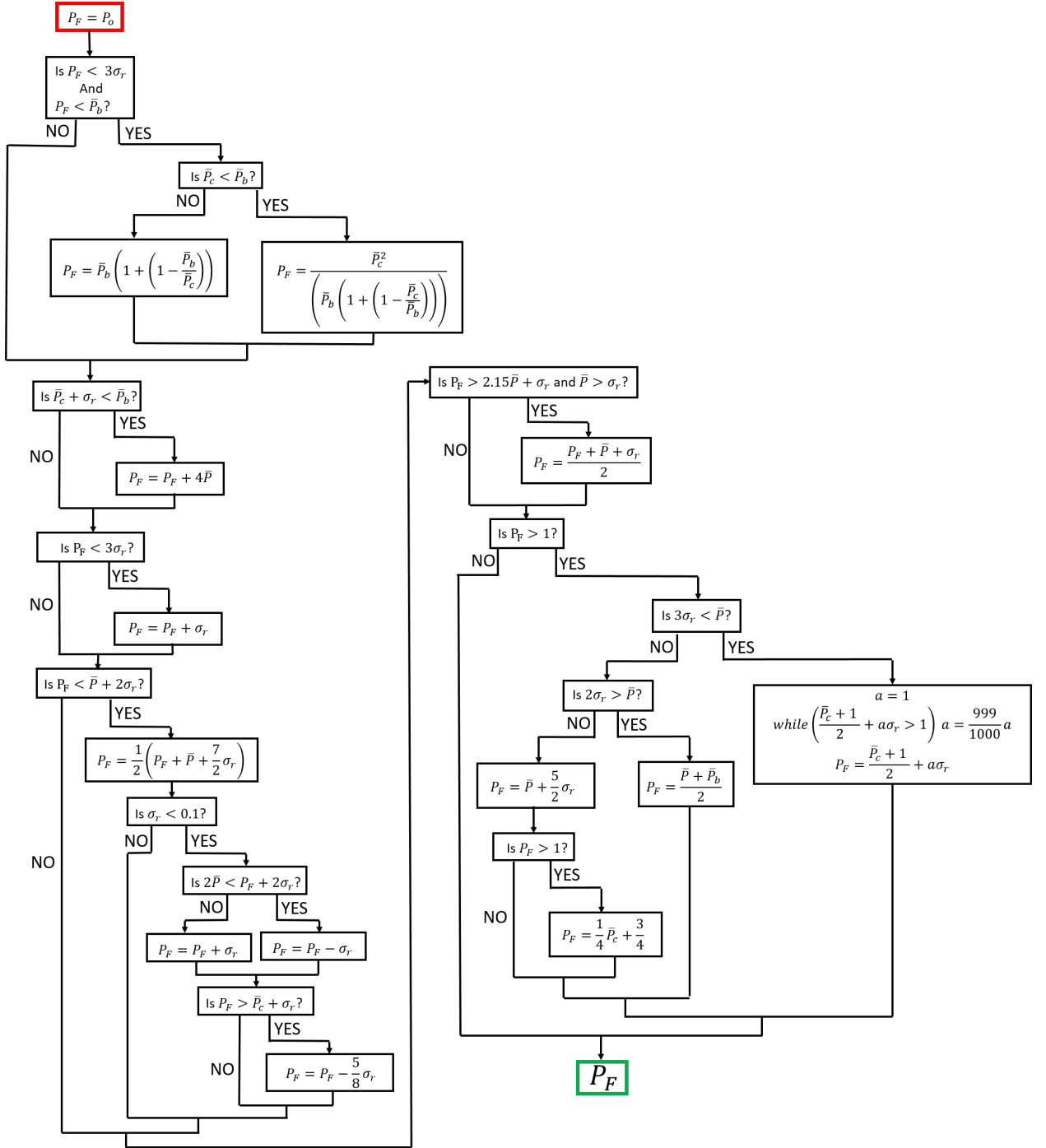


Figure 4: Thresholding logic for calculating the final binary threshold, P_F .

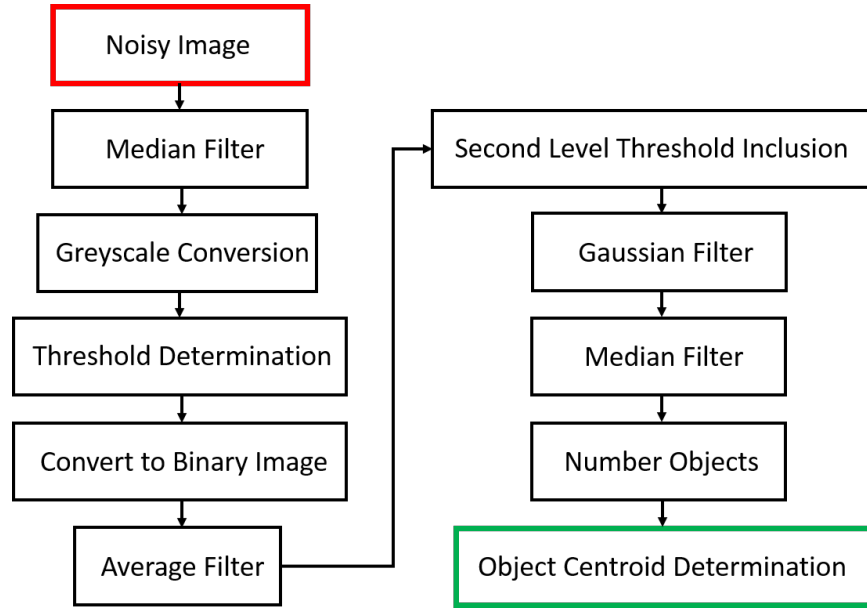


Figure 5: Noise cancellation, object determination, and object centroid scheme flow chart

$$\bar{P}_c = \frac{\bar{P} + 1}{2} \quad (14)$$

where \bar{P}_c can be used to estimate a peak location value, \bar{P}_b , if in the event of a result of no peaks. This can be found as

$$\bar{P}_b = \frac{\bar{P}_c}{2} \quad (15)$$

Another value needed, is the average row standard deviation of the NGSI, σ_r . This should not be confused with the total standard deviation of the NGSI. The average row standard deviation is found by

$$\sigma_r = \frac{1}{y_{pix}} \sum_{i=1}^{y_{pix}} \sqrt{\frac{1}{x_{pix}} \sum_{j=1}^{x_{pix}} (W_n(i, j) - \bar{P})^2} \quad (16)$$

Using P_o and the variables from Equations 12 to 16, a threshold, P_F can be found that will best find the objects of interest. Figure 4 shows the logic for determining a final threshold. A second level threshold is calculated for use within the algorithm. This is found by

$$P_2 = \frac{P_o + P_F}{2} \quad (17)$$

By using filtering logic and steps depicted in the flow chart of Figure 5, the noise elimination, object detection, and centroid locations can be found. An illustration of object detection and cen-

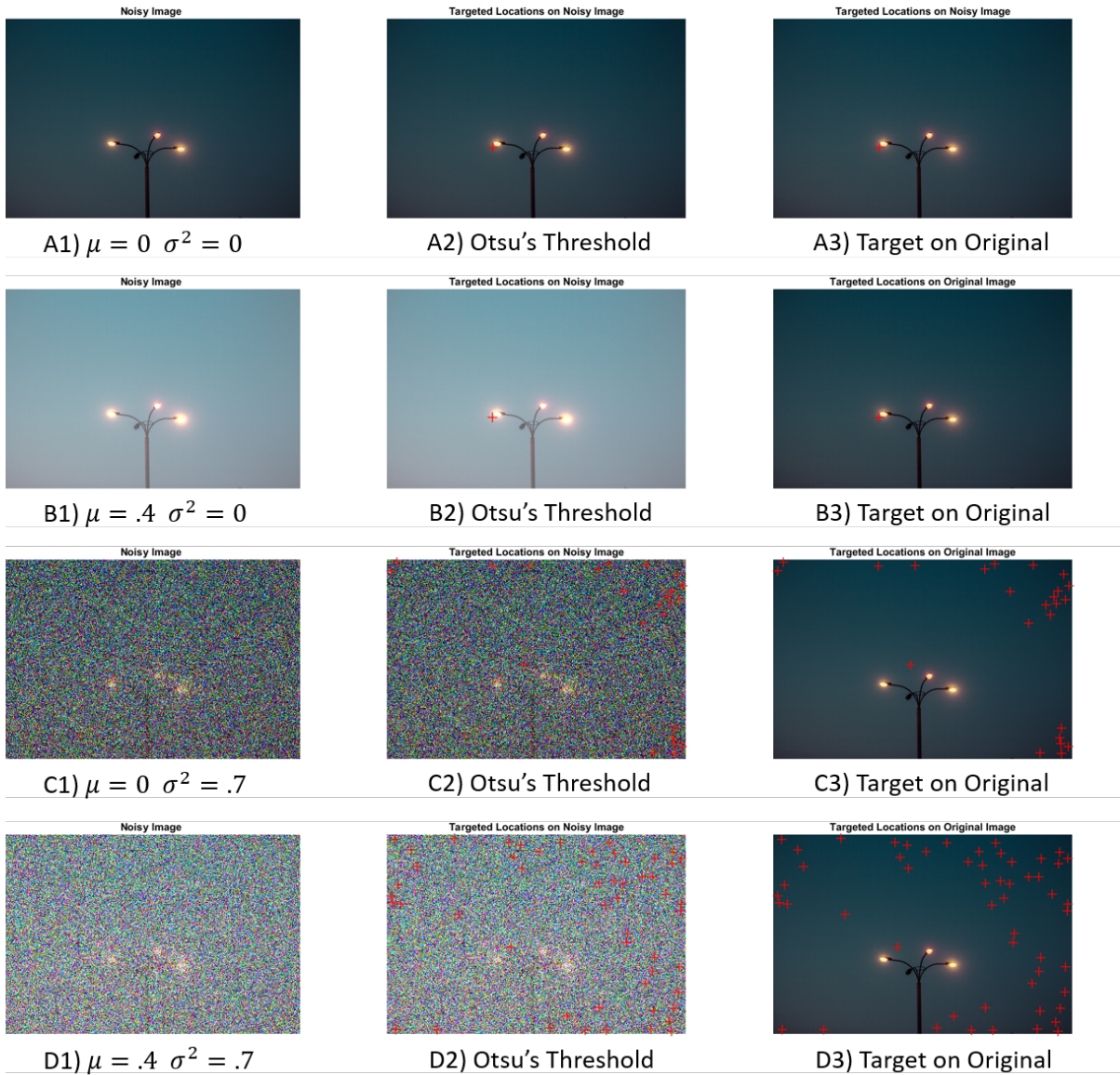


Figure 6: Otsu's Method of Threshold being used for various degrees of random Gaussian noise. Left image specifies noise addition, middle is detected objects centroids in the noisy image, right depicts targeted locations on original image. Noise was added using the `imnoise` function of Matlab. Original image courtesy of Angelina Litvin on <https://stocksnap.io/photo/U4JKNI8126>

troiding using Otsu's method as well as the thresholding described here can be found in Figures 6 and 7. In these images, zero mean random Gaussian noise, with differing standard deviations is implemented. The brighter objects in the scene are objects of interest, since this is mostly likely to be the situation in space. As it can be seen, Otsu's Method fails to have a threshold which properly separates the brighter objects from the rest of the image. The thresholding algorithm presented here is not guaranteed to detect all bright objects, but may also include random areas of higher valued pixel clusters. A pixel area comparison would be needed to establish if the object detected is a product of the noise or the actual object of interest. The case shown in Figure 7 does however, detect the

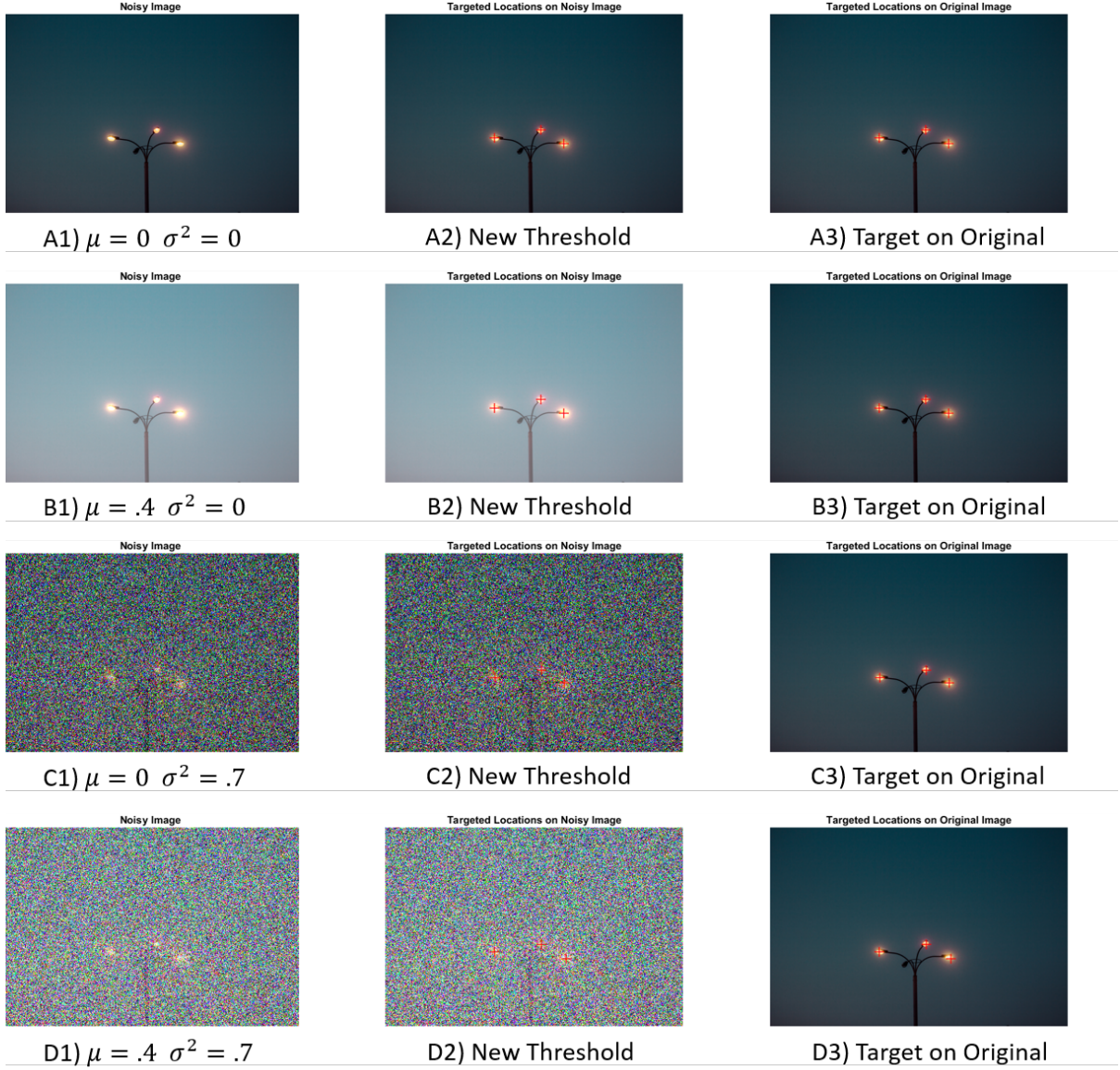


Figure 7: Otsu's method of threshold being used for various degrees of random Gaussian noise. Left image specifies noise addition, middle is detected objects centroids in the noisy image, right depicts targeted locations on original image. Noise was added using the `imnoise` function of Matlab. Original image courtesy of Angelina Litvin on <https://stocksnap.io/photo/U4JKNI8126>

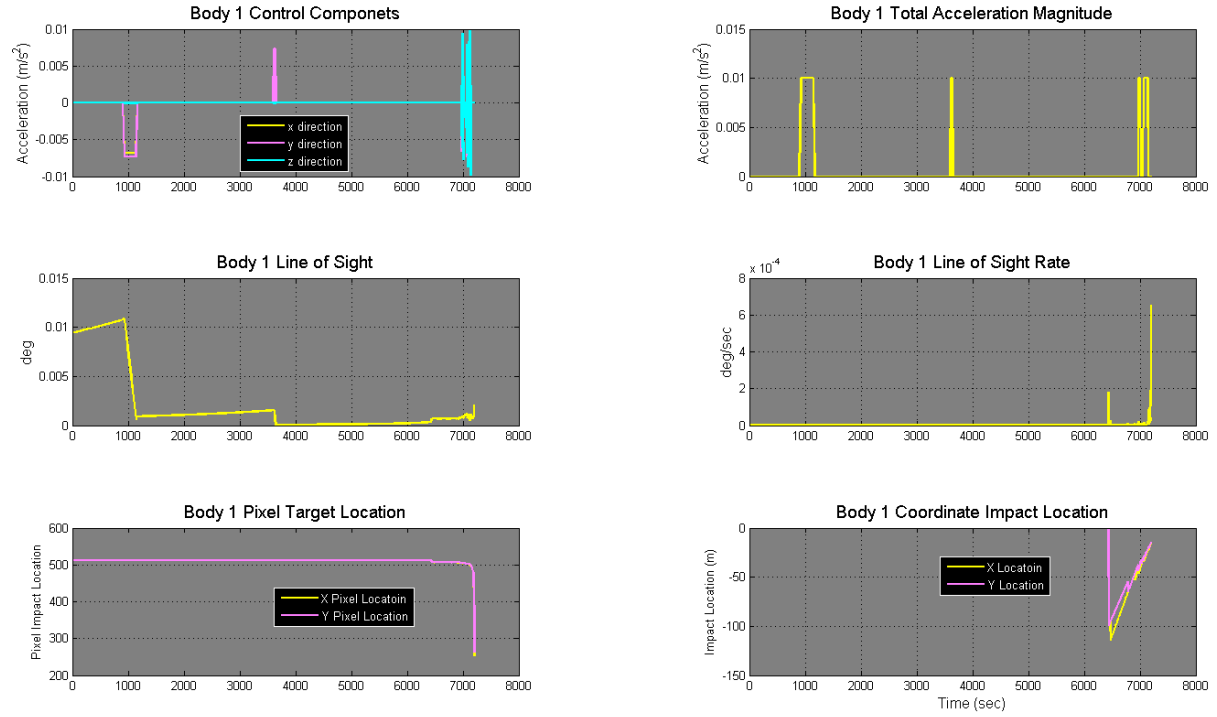


Figure 8: Control accelerations and mission variables with regards to one of the KEI's using unfiltered camera information

three bright lights of interest. In addition, implementation of the Local Area Signal-to-Noise Ratio (LASNR) algorithm given in [17] could help to further confirm exact objects of interest and object segmentation. However, the LASNR has not demonstrated its full capabilities when the image is diluted by substantial quantities of noise.

SIMULATIONS AND RESULTS

Simulations were ran using the same scenario as presented in [2], except for incorporating multiple impactors. Both infrared sensor cases and visual sensor cases are presented. During the simulations, it was found that taking pure camera data resulted in control acceleration jitter. Jitter was due to the impact locations changing pixel value, which at greater distances from the asteroid, will change the amount of change the LOS vector undergoes. To remedy this situation, a five sample averaging filter was implemented on the calculated impact locations. The calculated LOS no longer had the sharp changes due to the changing of pixels once this filter was incorporated. However, this does cause a delay when large changes are present. An example of the commanded control acceleration components for an unfiltered sequence of images can be seen in Figure 8, which is in reference to one of the kinetic-energy impactors.

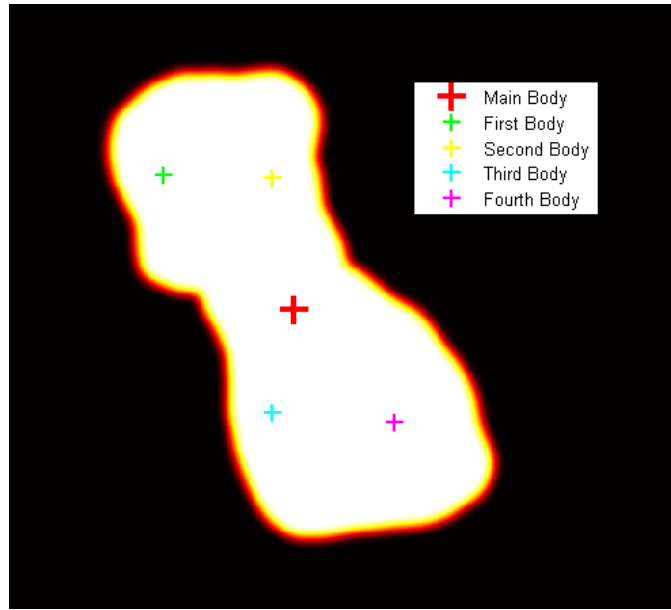


Figure 9: Predicted impact locations using an infrared sensing device.

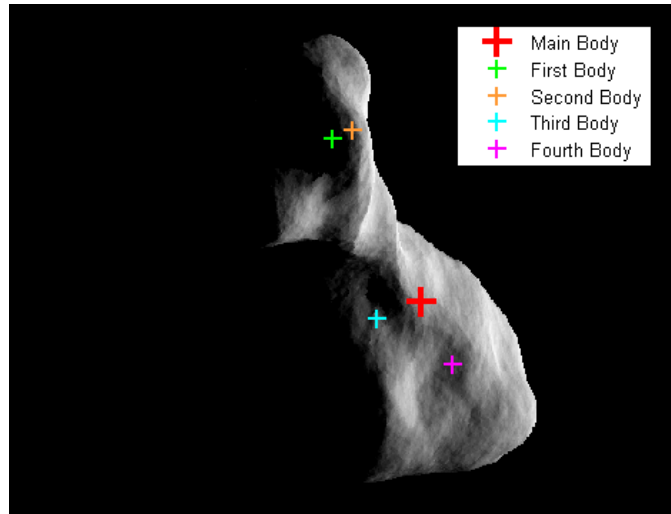


Figure 10: Predicted impact locations using a visual sensing device.

Noiseless Image for MKIV

The MKIV concept, using a noiseless image, implements a five impactor system. This consists of four KEI's and the CV, which contains the target sensing device and will be used as the fifth impactor. All of the four kinetic-energy impactors target locations are distributed on the body. In addition, the CV spacecraft targets the COF or COB. Figure 9 and Figure 10 show the predicted impact locations on a scaled model (100 m) of 216 Kleopatra corresponding to a simulated infrared image and a simulated visual image.

As it can be seen in Figures 9 and 10, the impact locations on the infrared image are distributed over the entire target body, while the impact locations on the visual image are limited by the il-

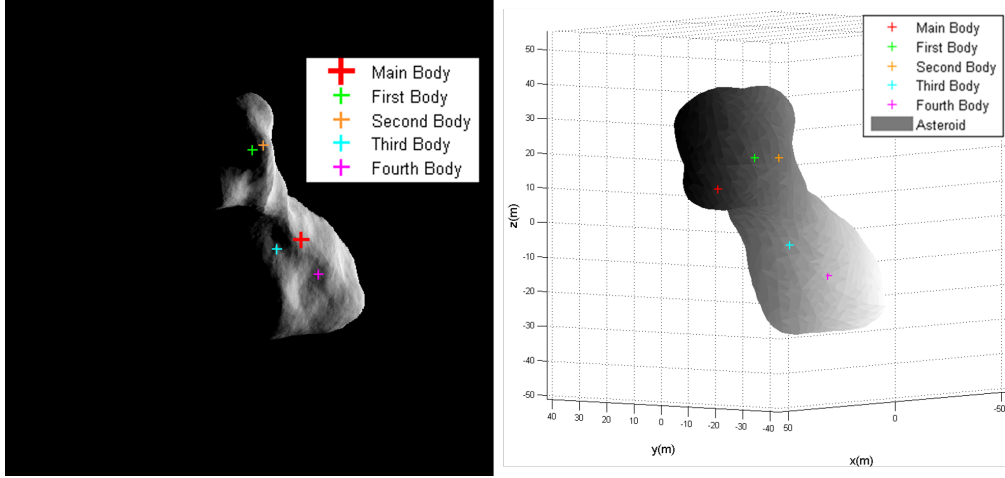


Figure 11: Predicted impact locations (left) and actual impact locations (right) using a visual sensing device.

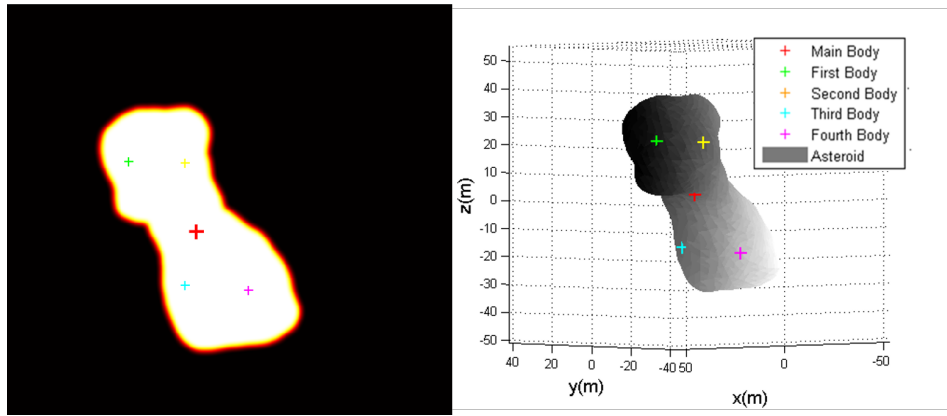


Figure 12: Predicted impact locations (left) and actual impact locations (right) using an infrared sensing device.

lumination of the asteroid's surface. Actual impact locations and a comparison with the targeted locations can be seen in Figure 11 and Figure 12. As the figures show, the impact locations on the body failed to impact precisely where targeted. This is due to the thrusters no longer being active when the KEIs are 60 seconds before impact. By doing so, it causes a targeting jitter while maintaining marginal accuracy in impact location.

All KEIs perform terminal guidance thrusting maneuvers. For ease, solely the first KEI will be shown. This is due to a comparison with the first body of the unfiltered case. An illustration of the mission components can be seen in Figure 13. As shown in this figure, the KEIt does not have an uncontrollable amount of system jitter. This can be compared with the identical KEI using unfiltered camera information, which is depicted in Figure 8.

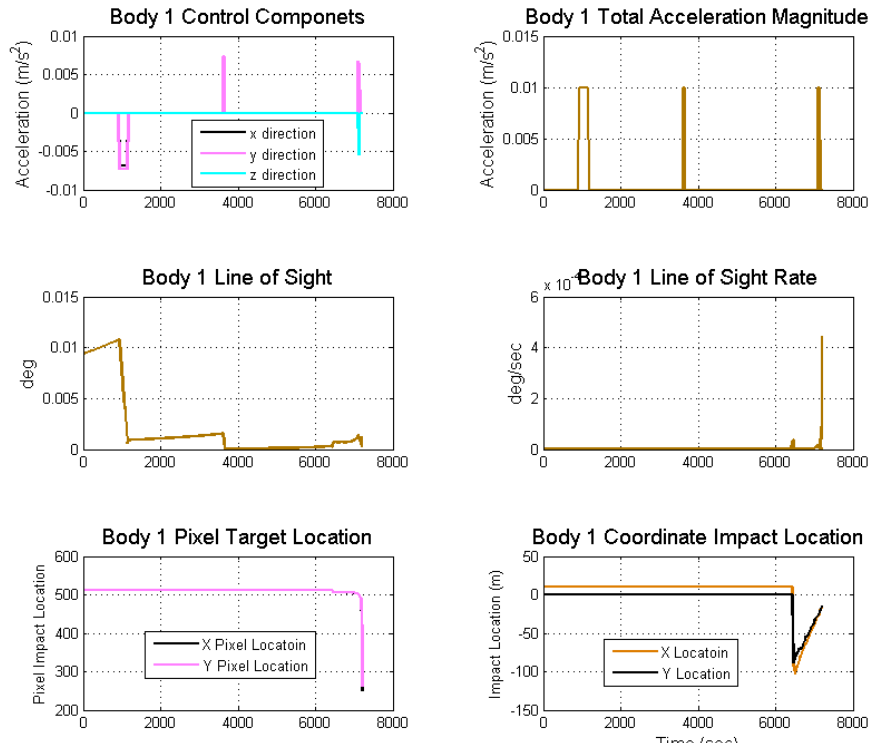


Figure 13: Control accelerations and mission variables of the KEI using filtered camera information.

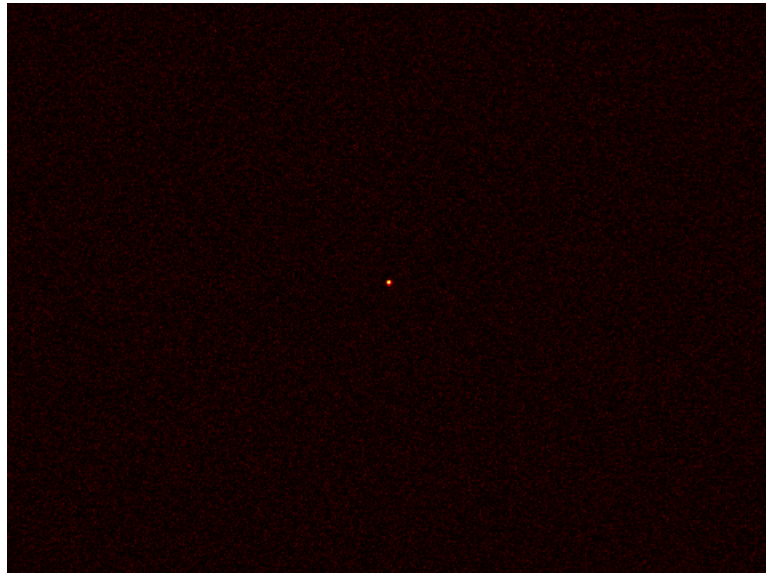


Figure 14: Simulated infrared image at approximately 2 hours from iimpact with a signal-to-noise ratio of approximately 22.

Noisy Image for MKIV

A similar mission scenario is conducted, where the KEI has thruster firings until 30 second before the final impact, using a simulated infrared camera with the addition of camera noise. A simulated

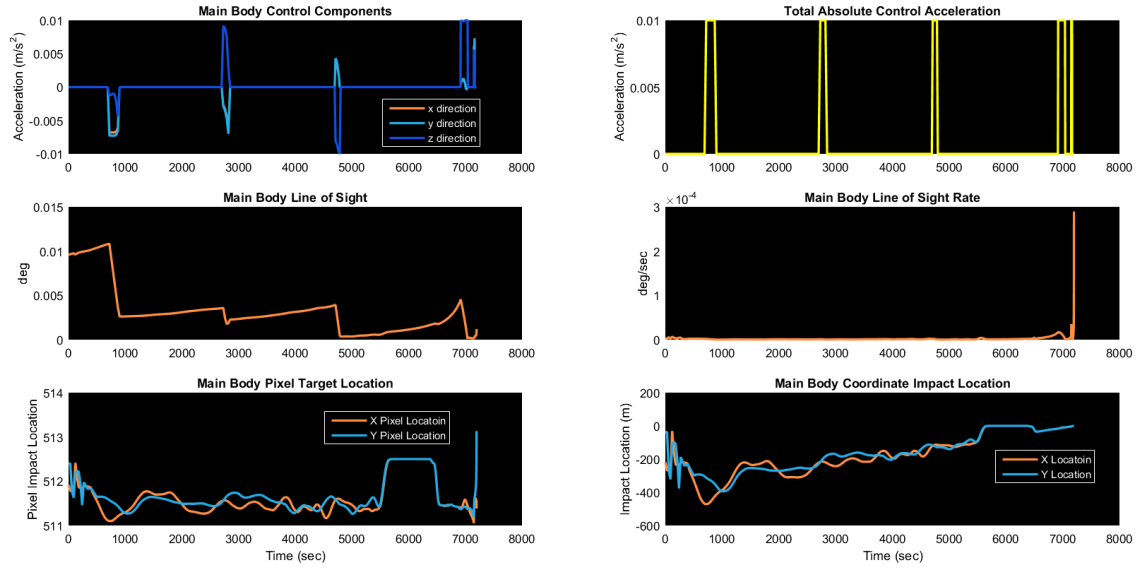


Figure 15: CV control accelerations and mission variables using filtered camera information.

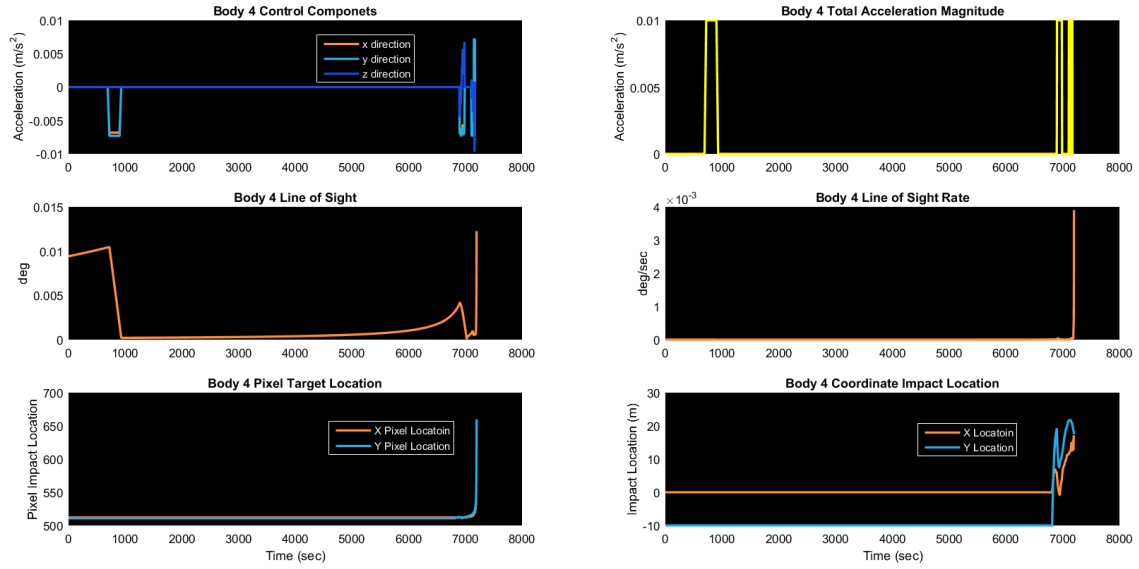


Figure 16: KEI-4 control accelerations and mission variables using filtered camera information.

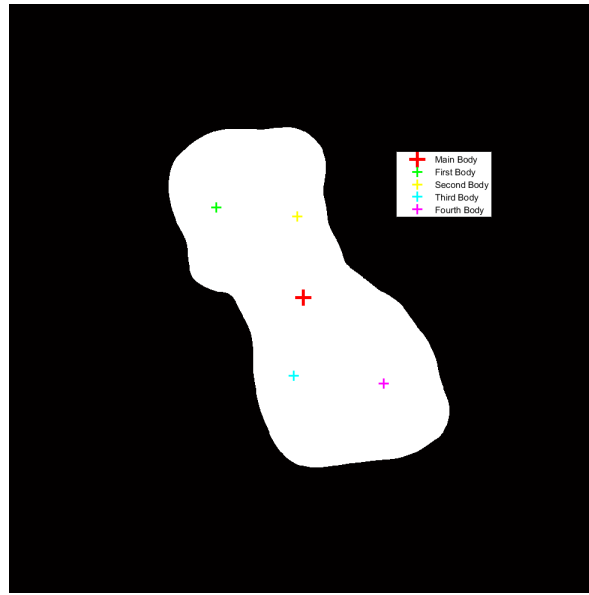


Figure 17: Object blob detection and targeted impact locations.

image at 2 hours before asteroid intercept can be seen in Figure 14. At this point, the asteroid on the image array has a signal-to-noise ratio of approximately 22. Digital image processing schemes are used to eliminate the noise caused by the asteroid and detector. Object blob detection and noise elimination is completed by the threshold method described in this paper.

Due to this thresholding, the impact locations may vary slightly. The actual target location, commanded accelerations, and other mission points of interest are shown in Figure 15. It can be seen that the information for the impact location is not constant, but has undergone an averaging filter such that the guidance scheme will not react to the original sharp changes in location caused by target location pixel jumping. By doing so, however, the averaging filter creates a delay in the information, which may cause the intercepting space craft to miss the target. If this situation were simulated, a weighted averaging smoothing scheme could be used. The depiction of one of the KEI's can be seen in Figure 16, which shows similar time histories to that of the CV. This KEI uses a weighted average due to needing to shift impact location when the asteroid begins to be resolved. A delay in the actual impact location could cause a failure in intercepting the target.

After the image undergoes thresholding, the targeted locations for the detected blob object are found by using the same method for a noiseless system. The targeted impact locations for the CV and KEI's are shown in Figure 17. It can be seen that this image is binary; either white or black. The white indicates the object. These impact locations are very similar to the locations found by the noiseless system since the blob detected is of similar shape to that of the actual asteroid. Information shown in Figures 15 to 17, along with other KEI's information, result in asteroid intercept. Asteroid intercept locations can be seen in Figure 18, where the colored pluses indicated a KEI or the CV. All interceptors impact the small, 100 meter asteroid. Not all crafts intercept at the targeted locations, which is due to the average filtering, triggering scheme, and image resolution at the time of thrusters turning off.

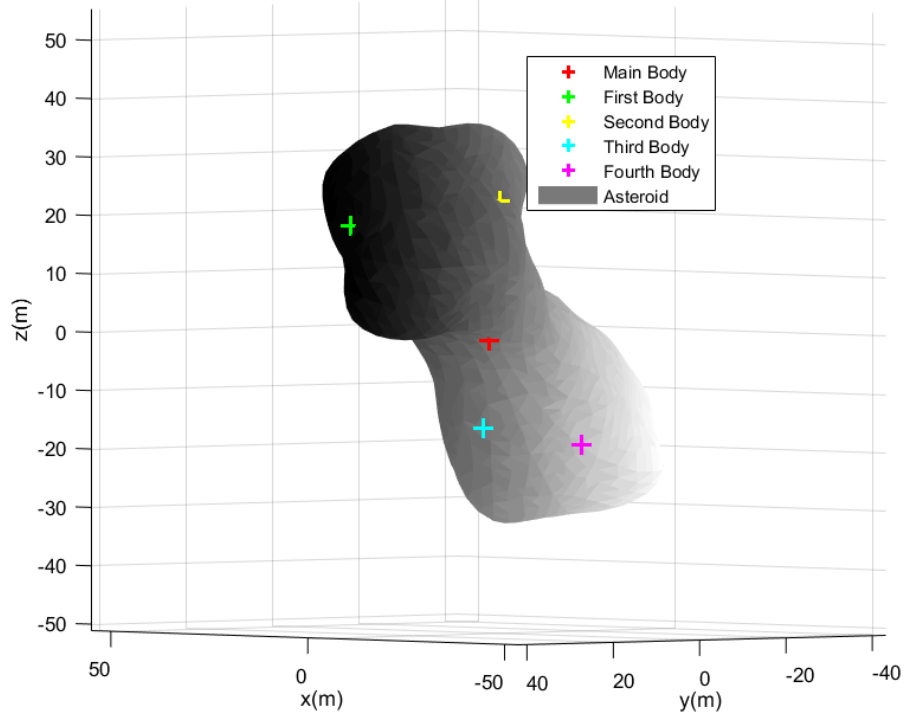


Figure 18: CV and KEI's impact location on a scaled 216 Kleopatra (100 m diameter).

FUTURE WORK

While impacting one target using multiple KEIs is a starting point of our research, future work will involve the incorporations of targeting and impacting multiple targets using a single or multiple camera system implemented on each KEI. The proposed scheme would include the use of object recognition for multiple images. Since this scheme uses blob detection, Hu's moments could be used to determine common objects in multiple images.

CONCLUSION

This paper has described a new non-nuclear MKIV (Multiple Kinetic-Energy Impactor Vehicle) system that can fragment or pulverize small asteroids (< 150 m) detected with short mission lead times (< 10 years). A brief description of the image segmentation, image thresholding, and impact-location predictions on the target using image processing on a mono-camera system has been presented. It was assumed that terminal guidance and control commands can be generated from the main carrier vehicle for all other KEIs. It has also been shown, through simulations, that the MKIV system can successfully intercept a target asteroid that is as small as 100 meters in diameter using camera data.

REFERENCES

- [1] Pitz, A., Kaplinger, B., Vardaxis, G., Winkler, T., and Wie, B., "Conceptual Design of a Hypervelocity Asteroid Intercept Vehicle (HAIV) and Its Flight Validation Mission," *Acta Astronautica*, 94, 2014, pp. 42-56.

- [2] Lyzhoft, J. et al., "GPU-Based Optical Navigation and Terminal Guidance Simulation of a Hypervelocity Asteroid Impact Vehicle (HAIV)," AIAA-2013-4966, AIAA Guidance, Navigation, and Control Conference, Boston, MA, 2013.
- [3] Lyzhoft, J. and Wie, B., "A New Terminal Guidance Sensor System for Asteroid Intercept or Rendezvous Missions," IAA-PDC 15-03-10, 4th IAA Planetary Defense Conference, Frascati, Rome, Italy, April 13-17, 2015.
- [4] Wie, B. "Hypervelocity Nuclear Interceptors for Asteroid Disruption," *Acta Astronautica* 90, 2013, pp. 146-155.
- [5] NATIONAL AERONAUTICS AND SPACE ADMINISTRATION, Deep Impact Launch, 2005.
- [6] Kubitschek, D. G., "Impactor Spacecraft Encounter Sequence Design for the Deep Impact Mission," 2005.
- [7] Strickland, B. R., and Lianos, D. P., "A Midcourse Multiple Kill Vehicle Defense against Submunitions." AIAA Defense and Space Programs Conference and Exhibit, Huntsville, AL, September 23-25, 1997. Vol. 9714, 1997.
- [8] Payton, G., "Advanced Concepts in Missile Defense." *The George C. Marshall Institute* (2005): 14-20.
- [9] Williams, D. S., Pflibsen, K., and Crawford, T., "Multiple Kill Vehicle (MKV) Interceptor and Method for Intercepting Exo and Endo-Atmospheric Targets," U.S. Patent No. 7,494,089. 24 Feb. 2009.
- [10] Leal, M., Baker, T., and Pflibsen, K., "Multiple Kill Vehicle (MKV) Interceptor with Autonomous Kill Vehicles," U.S. Patent No. 7,494,090. 24 Feb. 2009.
- [11] Wie, B. et al., "Non-Nuclear MKIV (Multiple Kinetic Impactor Vehicle) Mission Concept for Pulverizing Small (50-150 m) Asteroids with Short Warning Times," AAS 15-567, AAS/AIAA Astrodynamics Specialist Conference, Vail, CO, August 9-13, 2015.
- [12] Zimmerman, B. et al., "A GPU-Accelerated Computational Tool for Asteroid Disruption Modeling and Simulation," AAS 15-568, AAS/AIAA Astrodynamics Specialist Conference, Vail, CO, August 9-13, 2015.
- [13] Lyzhoft, J., Basart J., and Wie B., "A New Terminal Guidance Sensor System for Asteroid Intercept or Rendezvous Missions," *Acta Astronautica* 119, 2016, pp. 147-159.
- [14] Box, G. E. P., and Mervin, M. E., "A Note on the Generation of Random Normal Deviates," *The Annals of Mathematical Statistics* 29, No. 2 1958, pp. 610-611.
- [15] Otsu, N., "A Threshold Selection Method from Gray-Level Histograms," *Automatica*, 11(285-296), 1975, pp.23-27.
- [16] Huang, D-Y, Lin, T-W, and Hu, W-C, "Automatic Multilevel Thresholding Based on Two-Stage Otsu's Method with Cluster Determination by Valley Estimation." *ICIC International Journal of Innovative Computing, Information and Control* 7 (2011): 5631-5644.
- [17] Kegelmeyer, L. M. et al., "Local Area Signal-to-Noise Ratio (LASNR) Algorithm for Image Segmentation," *Optical Engineering+ Applications*, International Society for Optics and Photonics, 2007.